Open access • Journal Article • DOI:10.1016/J.JCIS.2018.12.054

A direct route to activated two-dimensional cobalt oxide nanosheets for electrochemical energy storage, catalytic and environmental applications

José M. Munuera, Juan I. Paredes, Silvia Villar-Rodil, Sergio García-Dalí ...+3 more authors

Institutions: Spanish National Research Council

Published on: 15 Mar 2019 - Joint International Conference on Information Sciences

Topics: European union

A direct route to activated two-dimensional cobalt oxide nanosheets for electrochemical energy storage, catalytic and environmental applications

J.M. Munuera,* J.I. Paredes,* S. Villar-Rodil, S. García-Dalí, A. Castro-Muñiz, A. Martínez-Alonso, J.M.D. Tascón

Instituto Nacional del Carbón, INCAR-CSIC, C/Francisco Pintado Fe 26, 33011 Oviedo, Spain

* Corresponding author: j.munuera@incar.csic.es

* Corresponding author: paredes@incar.csic.es

Abstract

Two-dimensional Co_3O_4 nanosheets have emerged as attractive materials for use in a number of relevant technological applications. To exhibit a competitive performance in such uses, however, their structure needs to be activated, which is frequently accomplished via post-synthesis reduction strategies that introduce oxygen vacancies and increase the number of active Co(II) sites. Here, we investigate a direct route for the synthesis of activated Co_3O_4 nanosheets that avoids reduction post-treatments, yielding materials with a high potential towards energy- and environment-related applications. The synthesis relied on an interim amorphous cobalt oxide material with nanosheet morphology, which upon calcination afforded Co_3O_4 nanosheets having Co(II) sites in quantities similar to those usually found for Co_3O_4 nanostructures activated by reduction post-treatments. When tested as electrodes for charge, the nanosheets demonstrated a competitive behavior in terms of both capacity and rate capability, e.g., a gravimetric capacity of ~293 mAh g^{-1} at 1 A g^{-1} with 57% retention at 60 A g^{-1} was measured for nanosheets calcined at 350 ºC. The materials were shown to be efficient catalysts for the reduction of nitroarenes (4-nitrophenol and 4-nitroaniline), outperforming other Co_3O_4 nanostructures, as well as effective adsorbents for the removal of organic dyes (methyl orange, methylene blue) from water.

Keywords: two-dimensional (2D) material, non–layered material, cobalt oxide, electrochemical charge storage, catalysis, dye adsorption.

1. Introduction

Spurred by the impressive advances in both fundamental and applied research on graphene and other two-dimensional (2D) materials of a layered nature (e.g., transition metal dichalcogenides such as MoS_2 and WS_2, hexagonal boron nitride, phosphorene or MXenes), the field of 2D materials has been continually evolving and maturing during the past decade.[1-5] In this regard, one of the most significant trends of the last few years has been arguably the surge of activity in a vast, relatively unexplored subset of materials from this family, namely the subset of non-layered 2D materials.[6–8] The latter can be defined as materials with a 2D morphology (nanosheets, atomically thin films, etc) the bulk, 3D counterparts of which do not possess a lamellar structure of weakly interacting (e.g., van der Waals type) atomic layers, but exhibit strong chemical bonds in the three spatial directions instead. Thus, in addition to boasting the general attractions of 2D materials, such as increased surface areas for interaction with the environment or distinct electronic properties derived from electron confinement, non-layered 2D materials (unlike layered ones) tend to possess sizable amounts of low-coordinated surface atoms, which makes them intrinsically more reactive and hence potentially useful in applications that rely on, e.g., redox reactions relevant in the areas of catalysis and energy conversion/storage.[8,9] The range of non-layered 2D materials currently under scientific scrutiny mainly includes transition and post-transition metal oxides (TiO_2, SnO_2, α-Fe_2O_3, Co_3O_4, etc) and hydroxides, noble and non-noble metals and their alloys (Au, Ag, Pd, Cu, etc), metal chalcogenides (e.g., Co_3S_4, CuS or CdSe), as well as perovskites.[6-8,10–12]

Among non-layered metal oxides in 2D form, Co_3O_4 has received in recent years significant attention with a view to practical applications, due to the low cost and toxicity, earth abundance and high corrosion stability of this oxide.[8,10,13] Furthermore,

thin (typically <10–20 nm) Co_3O_4 nanosheets exhibit large fractions of surface and near-surface metal sites with different oxidation states and high activities towards a number of redox and catalytic processes, making them an attractive material for use, e.g., as electrocatalysts for the oxygen evolution reaction[8,14–16] or as electrodes for supercapacitors[10,17–21] and Li-ion batteries.[10,22–25] Nonetheless, as is usually the case with many metal oxides, the performance of 2D Co_3O_4 nanosheets, and indeed of virtually any nanostructured form of Co_3O_4, in these and other applications is substantially limited by their poor electrical conductivity.[26,27] To address this issue, researchers have traditionally resorted to electrically conductive scaffolds of different types as supporting substrates of the metal oxides. Typical scaffolds include metal (Ni, Cu, etc.) foams and wires/nanowires, as well as graphitic carbon materials (carbon fibers, nanofibers and nanotubes, or graphene).[10,16,17,19,25,28–31] However, more recent efforts have targeted the intrinsic characteristics of the metal oxide, and thus have sought to finely tune its atomic-scale structure as a means of activating it towards the intended practical purpose, for instance through the introduction of defects or dopants, which includes the synthesis of mixed metal oxides based on cobalt (i.e., MCo_2O_4).[27,32–34] Also of particular relevance within this kind of strategy is the activation of Co_3O_4 nanosheets and other nanostructures (as well as many other nanostructured metal oxides) by post-synthesis reduction treatments that generate oxygen vacancies in the lattice and convert a fraction of the original Co(III) sites to the more (electro)catalytically active Co(II).[16,20,26,35–39] As a testament of its practical benefits, such an activation has led to Co_3O_4 nanosheets with much improved performance when used as, e.g., supercapacitor electrodes[20] or electrocatalysts for the oxygen evolution reaction.[16,39]

Although highly effective in enhancing the performance of 2D Co_3O_4 nanosheets, the aforementioned post-treatments are probably not the ideal option for activating this material with a view to its large-scale manufacturing and practical implementation, as they involve additional processing steps that require high temperatures and/or reducing agents. Furthermore, from an atom-economy perspective, a synthesis strategy whereby a large number of active Co(II) sites are originally present in the Co_3O_4 material is more attractive than one by which a full-fledged Co_3O_4 lattice is first generated only to remove a fraction of its oxygen atoms in a subsequent reduction step to increase the amount of Co(II). In this regard, we hypothesized that activated, i.e. Co(II)-rich, Co_3O_4 nanosheets could be directly accessed via appropriate synthesis routes without the need to resort to any kind of reduction post-treatment. Such a hypothesis was founded on the idea that in the bottom-up production of metal oxides from atomic/molecular precursors, the actual characteristics of the final (as well as intermediate) products should be determined to a significant extent by a number of synthesis parameters, such as the nature and amount of the precursors and solvents, the use of certain additives (e.g., surfactants), or the temperature and pH of the reaction medium.[40]

Following this line of exploration, we report here that activated 2D Co_3O_4 nanosheets with a remarkable performance towards several applications can be readily synthesized through a suitable procedure that obviates the need for any activation (reduction) post-treatment. The reported strategy bases on a general procedure recently developed by Sun *et al.*[41] and relies on the use of an interim material with nanosheet morphology that can be viewed as an amorphous cobalt oxide having an almost complete dominance of Co(II) sites. Subsequent calcination of this material at properly chosen temperatures afforded nanocrystalline Co_3O_4 nanosheets that retained a high fraction of Co(II) sites. When tested as electrodes for electrochemical charge storage,

the activated nanosheets outperformed many other activated and non-activated Co_3O_4 nanomaterials that have been previously studied for such a purpose, and they also exhibited a competitive performance as non-noble metal-based catalysts for the reduction of nitroarenes and as adsorbents for organic pollutants (dyes) from the aqueous phase. Such results demonstrate the potential advantages of these activated Co_3O_4 nanosheets application-wise.

2. Results and discussion

2.1. Rationale of the proposed route and characteristics of the starting solvothermal nanosheets

Fig. 1 shows a schematic representation of the rationale behind the proposed strategy for directly accessing activated Co_3O_4 nanosheets, avoiding the need for activation (reduction) post-treatments. The bottom-up synthesis of 2D Co_3O_4 nanosheets, as well as of Co_3O_4 in other nanostructured forms (e.g., 0D nanoparticles or 1D nanorods) generally relies on a solvothermal step carried out at a moderately low temperature (usually < 150 ºC), whereby a molecular or ionic cobalt precursor species is converted under basic conditions to α- or β-phase cobalt hydroxide (path A in Fig. 1).[40] The latter is then transformed to cobalt oxide through calcination at typical temperatures in the 250–500 ºC range. This process normally affords Co_3O_4 materials with a limited concentration of active sites, i.e., Co(II) centers that are frequently associated to oxygen vacancies in the lattice, so that a subsequent reduction post-treatment is required to attain a substantial amount of such active sites.[16,20,35,36,42,43] Typical reduction strategies include high temperature annealing in a hydrogen-containing atmosphere or the use of proper reducing agents, such as $NaBH_4$, in the liquid phase. On the other hand, it has been suggested that cobalt oxide already starts to form at temperatures around 150 ºC or

even lower, although this depends on the specific synthesis conditions.[44–47] For example, the presence of a small amount of water in the solvothermal medium has been shown to trigger the structural evolution from the hydroxide to the oxide phase at moderate temperatures.[48] Therefore, we surmised that conducting the solvothermal step under appropriate conditions (e.g., temperature slightly above 150 ºC in the presence of a small amount of water) could allow the cobalt precursors to react and develop past the hydroxide stage into an incipient cobalt oxide material (path B in Fig. 1).[48,49] Due to the relatively low temperature of the solvothermal step, such an oxide (before calcination) should possess a highly disordered or even amorphous structure, and thus should exhibit a large concentration of active (defect) sites. Upon calcination, the solvothermal oxide should evolve towards (nano)crystalline Co_3O_4. However, owing to its expected higher stability relative to the hydroxide phase, the structural evolution of this oxide (and in particular, the healing of its defect sites) could be somewhat limited, especially at moderate calcination temperatures. As a result, the final Co_3O_4 material would retain a large number of the defect sites originally present in the solvothermal oxide and hence would be directly obtained in an activated state, hence circumventing the need for any activation post-treatments.

Building on this idea, we synthesized 2D Co_3O_4 nanosheets using a solvothermal route at a relatively high temperature (170 ºC) that yielded an interim cobalt oxide, which was then calcined at different temperatures (250, 350 and 450 ºC) to give a range of final Co_3O_4 materials having a substantial degree of activation. The solvothermal step was based on a general procedure recently developed by Sun *et al.*[41] and was carried out in a mixed ethanol/water solvent with cobalt (II) acetate tetrahydrate as the precursor and hexamethylenetetramine as a base, in the presence of the polymeric surfactant Pluronic P123 as well as ethylene glycol as a co-surfactant (see Experimental section

for details). It was reported that with the assistance of ethylene glycol, the Pluronic P123 surfactant forms an inverse micellar phase of a lamellar structure, which confines the oligomerization and assembly of the cobalt precursor in a 2D space and thus promotes the formation of a product with nanosheet morphology.[41,50] In the work by Sun *et al.*[41] the synthesis of Co_3O_4 nanosheets is reported amidst several examples in the more general framework of transition metal oxide. As long as cobalt oxide is concerned, the focus is on the characteristics of the final, calcined product at a particular temperature (400° C), no information being provided on the characteristics of the non-calcined solvothermal product or the calcined products obtained in intermediate stages of the process. Such an information is reported here in detail. As illustrated in Fig. 2a, the solvothermal method developed by Sun *et al.*[41] yielded a pale green powdery solid (left) that could be readily dispersed in water by means of a mild sonication step (right). Field emission scanning electron microscopy (FE-SEM) indicated that the as-prepared solid was a collection of large (up to several hundreds of micrometers) and relatively thin (~5–10 μm) plates (Fig. 2b). Closer inspection of their edges revealed that the plates were of a highly stratified nature (Fig. 2c), this being consistent with the formation of the solid within the confinement of a lamellar micellar phase. Individual nanosheets could be readily detached from the plates in large numbers through mild sonication, the 2D character of which was made apparent by imaging them with scanning transmission electron microscopy (STEM). Nanosheets that were highly transparent to the electron beam and exhibited many wrinkles and folds could be noticed (Fig. 2d). Apart from these morphological features, these nanosheets did not display any internal structure and appeared essentially featureless in the images, with their typical lateral sizes ranging between several hundreds of nanometers and a few

micrometers. Furthermore, atomic force microscopy (AFM) indicated that their thickness was typically ~3–5 nm (Fig. 2e).

The solvothermally obtained pale green nanosheets could not be assigned to a cobalt hydroxide phase. α- and β-phase cobalt hydroxides, which are generally associated to dark green (or deep blue) and pink solids (see Fig. S1 in the Supporting Information), respectively. In fact, their color was that characteristic of cobalt oxide with the metal in the divalent state (CoO).[51] Of course, these colored substances can be distiguished on the basis of their optical absorption spectra. Specifically, α-$Co(OH)_2$ displays a strong doublet band in the 600–700 nm wavelength range, arising from Co(II) in tetrahedral coordination with hydroxide anions, together with an additional, relatively weak band in the 450–550 nm region [Co(II) in octahedral coordination], whereas only the latter is present in β-$Co(OH)_2$.[52–55] Such bands were completely absent from the UV-vis absorption spectrum of the solvothermal product (Fig. 3a), which was characterized by a sharp peak at around 200 nm along with a relatively broad shoulder in the 300–450 nm region. Indeed, these features were very similar to those previously reported by other authors for several cobalt oxide nanostructures (including nanosheets),[56,57] suggesting that the present solvothermal solid was also a cobalt oxide predominantly in an oxidation state of +2. It must be noted that although α-$Co(OH)_2$ has been included in this discussion for completeness, it is not strictly $Co(OH)_2$ as it contains layers of anions other than hydroxide (such as nitrate, carbonate, chloride…) [58]. Consequently, during the synthesis of our materials, in the absence of such anions, such substance could not possibly have formed.

The X-ray diffraction (XRD) pattern of the solvothermal material (not shown) was completely featureless, pointing to a poorly crystalline or even amorphous structure. On the other hand, its Raman spectrum (Fig. 3b) was dominated by an intense peak located

at ~515 cm^{-1}, a relatively weak peak at around 450 cm^{-1} and two broad bands at ~690 and 1060 cm^{-1}. Collectively, these Raman features could not be unequivocally assigned to any crystalline, pristine cobalt oxide (CoO, Co_3O_4) or hydroxide phase,[59-62] or even to amorphous cobalt hydroxide.[63] Still, they were consistent with the presence of a highly defective oxide in which cobalt was mostly found in an oxidation state of +2. More specifically, it is known that the Raman spectrum of single-crystal, defect-free CoO only incorporates a broad and relatively weak band located at ~1060 cm^{-1}, which is ascribed to a second-order, two-phonon scattering process, while first-order processes are forbidden due to symmetry considerations.[61] In the presence of structural disorder in the CoO lattice, however, a number of first-order bands may appear in the 450–700 cm^{-1} region of the spectrum, in particular bands at ~510–540 and 450–480 cm^{-1},[61,64,65] this being similar to what was obtained with the solvothermal solid investigated here (Fig. 3b). We note that a sharp peak located around 670–690 cm^{-1} has also been frequently reported in the literature for CoO materials, but such a peak has been recently ascribed to Co_3O_4 generated by the partial oxidation of CoO due to laser-induced heating during the Raman measurement.[61] In our case, the solvothermal nanosheets exhibited a broad, weak band at ~690 cm^{-1}, suggesting that Co(III) was only present to a minimal extent in the solid. This result was consistent with the fact that the solvothermal synthesis was carried out at a moderate temperature (< 200 ºC) in a closed autoclave (i.e., with a limited supply of oxygen), so that conversion of the Co(II) precursor species to higher oxidation states should be difficult to come about.

X-ray photoelectron spectroscopy (XPS) provided further support to the aforementioned conclusion. The survey spectrum of the solvothermally derived nanosheets (see Fig. S2a in the Electronic Supplementary Material) revealed the presence of only cobalt, oxygen and carbon. The latter was mainly ascribed to the well-

known hydrocarbon contamination of surfaces (adventitious carbon) that so pervasively comes to light in XPS in the form of a C 1s band located at a binding energy of ~285 eV (Fig. S2b).[66] The high resolution Co 2p and O 1s core-level spectra of the sample are presented in Fig. 3c and d, respectively. We note that the Co 2p band is indeed a doublet, corresponding to Co $2p_{1/2}$ and Co $2p_{3/2}$ levels. However, both components contain the same information, so only the Co $2p_{3/2}$ region is shown in Fig. 3c for simplicity. The Co $2p_{3/2}$ band comprised a main peak located at a binding energy of ~780 eV, which in principle contains contributions from cobalt species in different oxidation states [including Co(III) at ~779.6 eV and Co(II) at ~780.9 eV], and a second, less intense peak at around 786 eV, which has been identified as a satellite band arising exclusively from Co(II) species[67] (see Fig. S3 in the Supporting Information). Fitting of the main peak with potential contributions from both Co(III) and Co(II) components led to a negligible contribution from the former species, indicating that cobalt was mostly (if not exclusively) present in an oxidation state of +2 in the solvothermal nanosheets. The O 1s band exhibited a rather symmetrical shape, suggesting that all the oxygen species in the material were essentially of the same type. Further, the position of this band (~531 eV) was consistent with that expected for oxygen in defective locations of cobalt oxides.[68] Therefore, taken together, the characterization results described above indicated that the solvothermal nanosheets synthesized by general procedure developed by Sun *et al.*[41] were essentially a highly defective or even amorphous Co(II) oxide with little, if any, contribution from Co(III) species.

2.2. Conversion of the solvothermal nanosheets to activated Co_3O_4 nanosheets

To convert the highly defective, solvothermal Co(II) oxide nanosheets to an activated Co_3O_4 phase, i.e., to Co_3O_4 nanosheets that retain a substantial amount of

Co(II) sites, the former were subjected to calcination under static air conditions at moderate temperatures (250, 350 and 450 ºC). In all cases, the pale green color of the starting solid changed to a blackish tone upon calcination, consistent with the emergence of the Co_3O_4 phase. Fig. 4 shows FE-SEM images of the products calcined at 250 (a), 350 (b) and 450 ºC (c). Unlike their non-calcined counterpart (Fig. 2b), these materials were made up of relatively loose clumps of randomly arranged, thin nanosheets. Furthermore, a closer inspection of individual nanosheets by STEM [Fig. 4d and g (250 ºC), e and h (350 ºC), f and i (450 ºC)] revealed substantial differences between the calcined and non-calcined samples. First, although the lateral size of the individual nanosheets did not appear to change significantly upon calcination, the calcined objects were much less transparent to the electron beam of the microscope and appeared to exhibit less wrinkles and folds (Fig. 4d-f). These features were clearly indicative of thicker and more rigid nanosheets. Indeed, AFM measurements (see inset to Fig. 4e) revealed the thickness of the calcined nanosheets to range typically between 5 and 15 nm. Second, the calcined nanosheets possessed a distinct internal structure, consisting of a more or less compact assembly of nanometric grains with scattered holes in-between, the latter becoming somewhat larger but less abundant at higher calcination temperatures (Fig. 4g-i). The grain size (generally ~8–15 nm, but tending to increase slightly with calcination temperature) was similar to the thickness of the nanosheets determined by AFM, suggesting that each individual nanosheet was made up of just one monolayer of grains.

We interpret the grainy structure of the calcined nanosheets to be a result of localized crystallization events taking place in the starting, amorphous solvothermal nanosheets during the heat treatment. In this process, Co_3O_4 nuclei would be initially generated at many random locations throughout the nanosheet, with their surrounding

amorphous phase acting as the source material for the growth of these nuclei into nanometer-sized grains. Owing to the isotropic, non-layered nature of the Co_3O_4 lattice, the individual nanocrystals should be expected to grow at similar rates along the three spatial directions, and in particular their growth along the direction perpendicular to the nanosheet should not be confined to the very small thickness (~3−5 nm) of the starting amorphous nanosheet. At the same time, however, this very small thickness should prevent the formation of multiple grains along the direction perpendicular to the nanosheet, because there would be a limited supply of source material along that direction. In consequence, the amorphous solvothermal nanosheet would be converted to a monolayer of interconnected Co_3O_4 nanocrystals, yielding nanosheets that could be thicker than their corresponding solvothermal oxide precursors, as it was indeed the case. The transformation of the amorphous solvothermal nanosheets into a thicker, monolayered assembly of nanometer-sized grains should also lead to the appearance of voids (holes) in the resulting nanosheets, which was observed in the STEM images as well.

Direct evidence for the crystallization of the solvothermal nanosheets upon calcination was obtained by XRD (Fig. 5a). Unlike the case of the starting nanosheets, the XRD pattern of which was completely featureless, the diffractogram of the calcined materials exhibited a peak located at ~36º (2θ), which could be assigned to the (311) reflection of the Co_3O_4 lattice (standard XRD data for Co_3O_4 are shown in Fig. S4).[16,36,69,70] The intensity of the (311) reflection, which is generally the most intense XRD peak observed in Co_3O_4 materials, rose with the calcination temperature, which was ascribed to a corresponding increase of crystallinity. However, the fact that other, rather intense peaks [e.g., (220) at ~31º, (511) at ~59º or (440) at ~66º] could not be clearly made out from the background noise pointed to a relatively limited

crystallization of the solvothermal nanosheets upon calcination. Nonetheless, the conversion of the latter to Co_3O_4 was corroborated by the emergence of the Raman signature peaks of the spinel phase (Fig. 5b). More specifically, the Raman spectra of the calcined nanosheets displayed five well–defined bands located at ~192, 470, 515, 610 and 672 cm^{-1}, which could be ascribed to three F_{2g}, one E_g and one A_{1g} vibrational modes of Co_3O_4.[59,65,69] It is worth noting that the position of these bands appeared somewhat downshifted (a few to several cm^{-1}) relative to what is commonly found for bulk and nanostructured Co_3O_4, a result that can be put down to the relatively poor crystallinity of the present calcined nanosheets.[20,70,71] The trend with calcination temperature of such downshift was that expected from the above results on cristallinity, i. e., the lower the calcination temperature, the larger the downshift. The UV-vis absorption spectrum of all the calcined samples (Fig. 5c) was also in agreement with that expected for Co_3O_4, which is mainly characterized by two broad bands centered at about 470 and 770 nm.[37,69] No clear trends with calcination temperature were found in this case.

To provide quantitative estimates of the degree of activation of these Co_3O_4 nanosheets, which is determined by the relative abundance of Co(II) sites, the XPS technique was employed. Fig. 5d shows the high resolution Co $2p_{3/2}$ core-level spectra for the samples calcined at the different temperatures. As could be anticipated, the intensity of the Co(II)-associated satellite band relative to the main peak at ~786 eV decreased significantly after calcination (compare with the spectrum of the non-calcined material in Fig. 3c), strongly suggesting that Co(II) was no longer the only cobalt species present in the nanosheets. In point of fact, as can be seen from Fig. 5d, the main peak could be fitted with a combination of Co(II) and Co(III) components. In the fitted spectra, the full width at half maximum of the former component was substantially

larger than that of its Co(III) counterpart (2.7 vs 1.7 eV), a result whose physical origin is grounded on the fact that Co(II) is an unresolved spin-triplet system, whereas Co(III) is a spin-singlet.[68] The Co(II)/Co(III) molar ratio of the samples, which is taken as a quantitative proxy of the degree of activation of Co_3O_4, was evaluated on the basis of the area of the corresponding cobalt components in the spectra, yielding values of ~1.4 for the nanosheets calcined at 250 and 350 ºC and ~1.3 for those calcined at 450 ºC, the degree of activation shows a slightly diminishing trend with calcination temperature. For ideal, stoichiometric Co_3O_4, a Co(II)/Co(III) ratio of 0.5 is expected. Nevertheless, the actual ratios determined in real Co_3O_4 materials synthesized using calcination temperatures below 500 ºC tend to be higher, with typical values lying in the 0.6–1.0 range.[16,20,42,71–73] On the other hand, activation of these materials through reduction post-treatments has been shown to further increase the Co(II)/Co(III) ratio to the 1.2–1.7 range.[16,20,42] Such results indicate that the Co_3O_4 nanosheets investigated here boasted a substantial degree of activation, even though no reduction post-treatment was applied to them, and therefore demonstrate a direct, simplified route to access this type of active material.

An increased fraction of Co(II) sites in Co_3O_4 should be associated to the presence of significant numbers of oxygen vacancies in the lattice. The latter can be indirectly detected in the XPS O 1s band of the sample, as the binding energy of 1s electrons from oxygen atoms neighboring oxygen vacancies (i.e., defect oxygen; ~531 eV) is known to be different to that from oxygen atoms located in unaltered regions of the lattice (i.e., lattice oxygen; ~529.5 eV).[67,68] Fig. 5e shows the high resolution O 1s core-level spectra of the calcined nanosheets, which revealed the presence of a significant amount of oxygen species of the former type, in addition to the expected Co_3O_4 lattice oxygen. We note, however, that a direct correlation between the area of the component associated to

defect oxygen in the O 1s band and the concentration of oxygen vacancies in the material cannot be possibly made. This is because the number of defect oxygen atoms that contribute to such a component should most likely be determined not only by the overall density of oxygen vacancies, but also by their specific spatial distribution (e.g., isolated vs clustered vacancies), which should be highly dependent on the history of the material.

2.3. Applications of the activated Co_3O_4 nanosheets

It is known that having an increased fraction of Co(II) sites in nanostructured Co_3O_4 materials can bring a number of advantages with a view to their use in practical applications. For instance, Co(II) centers associated to oxygen vacancies increase the electrical conductivity of Co_3O_4 through n-type doping of the lattice, which can be highly beneficial when used as an electrode in electrochemical energy storage and conversion devices,[35,39,42] and they have been identified as the main active site towards different (electro)catalytic reactions, such as the oxygen evolution reaction,[74] the electroreduction of CO_2[70] or the reduction of nitroarenes.[36] Furthermore, because extra Co(II) sites are associated to a local increase in electron density,[35] those sites present on the Co_3O_4 surface should exhibit enhanced interaction with certain foreign chemical species (e.g., molecules with electron-deficient groups), so that activated Co_3O_4 with high surface area (nanoparticles, nanosheets, etc) could also be an attractive material in adsorption processes. To explore the potential of the activated Co_3O_4 nanosheets investigated here in these application areas, we have examined their performance towards three specific uses, namely (1) as electrodes for electrochemical charge storage, (2) as catalysts for the reduction of nitroarenes (4-nitrophenol and 4-nitroaniline), and (3) as adsorbents of dyes (methyl orange and methylene blue) from the aqueous phase.

2.3.1 Electrochemical energy storage

The electrochemical charge storage experiments were carried out in a three-electrode configuration using the cobalt oxide samples supported onto graphite foil as the working electrode, a commercial activated carbon as the counter electrode and Hg/HgO as the reference electrode, with aqueous 6 M KOH as the electrolytic medium (see Experimental section for details).

Fig. 6a shows typical cyclic voltammograms (CVs) recorded at a potential scan rate of 10 mV s^{-1} for the non-calcined nanosheets as well as their counterparts calcined at different temperatures. The evolution of the CVs of the sample calcined at 350 ºC with increasing scan rate between 3 and 500 mV s^{-1} is presented in Fig. 6b, whereas the corresponding results for the other three samples are given in Fig. S6 of the Electronic Supplementary Material. Similar to what has been reported in the literature for Co_3O_4 materials,[75] the obtained CVs were dominated by intense oxidation and reduction peaks, indicative of a charge storage mechanism that is mostly reliant on Faradaic redox reactions occurring at the metal centers of the oxide. This type of behavior allowed us to categorize the present materials as having a battery-type response rather than a capacitor-type one,[75–77] where charge storage is mostly based on ionic intercalation into the electrode and not on the formation of an electrical double layer on its surface. Such a conclusion was further substantiated by the observation that the magnitude of the measured current for the oxidation peak located at 0.42–0.46 V vs Hg/HgO was directly proportional to the square root of the potential scan rate (i.e., $I \sim \nu^{1/2}$, where I is the oxidation peak current and ν is the scan rate), as can be seen in the inset to Fig. 6b. This square root dependence implied that the electrode capacity was controlled by diffusion

of the electrolyte ions into the material, which in turn was consistent with a battery-type behavior.[76]

Representative galvanostatic charge-discharge curves, in the form of voltage vs gravimetric capacity plots, recorded for the different cobalt oxide nanosheet samples at a current density of 10 A g^{-1} are shown in Fig. 6c, while charge-discharge curves for the sample calcined at 350 ºC measured at current densities between 1 and 60 A g^{-1} are presented in Fig. 6d. Charge-discharge curves for the other three materials can be found in Fig. S7 of the Electronic Supplementary Material. As expected for battery-type electrodes, the galvanostatic curves were highly non-linear, exhibiting large regions of slowly varying potential, i.e., plateaus. For example, the plateaus in the discharge curves of Fig. 6d were located in the 0.3–0.4 V range (vs Hg/HgO), which was consistent with the potential at which reduction of the cobalt centers took place as deduced from the reduction peaks in the CVs of this sample (Fig. 6b). From the discharge curves we determined the gravimetric capacity delivered by the materials, the values of which are plotted in Fig. 6e as a function of current density. At low current densities, all the samples (both calcined and non-calcined) were seen to deliver similar capacities (e.g., between 265 and 295 mAh g^{-1} at 1 A g^{-1}). However, significant differences emerged in terms of their rate capability, with the non-calcined nanosheets displaying the poorest performance. More to the point, the capacity values for the latter dropped markedly with increasing current density (particularly in the range up to 30 A g^{-1}), yielding a capacity retention of only ~18% at the highest current density of 60 A g^{-1}. By contrast, the reductions in capacity for the calcined nanosheets were much more moderate, with retention values of about 43, 57 and 49% at 60 A g^{-1} for the materials calcined at 250, 350 and 450 ºC, respectively. Moreover, the coulombic efficiency of the nanosheets, defined as the ratio between the charge delivered in a discharge cycle

and the charge stored during a charging cycle, was ~85–90% at a current density of 1 A g^{-1} and approached 100% at 60 A g^{-1}. Furthermore, their stability as electrodes was tested by recording consecutive galvanostatic charge/discharge cycles. After 3000 cycles, ~95% of the initial capacity of the electrodes was retained with the nanosheets calcined at 350 °C and 450 °C, whereas the capacity retention was around 105% for the material calcined at 250 °C and 115% for the non-calcined material (Fig. S8 in the Electronic Supplementary Material). Such increases in capacity with cycling are not unusual in electrochemical energy storage devices of metal oxides, and can be ascribed to the conditioning of the materials upon the charge-discharge cycles, especially those with a poorer crystalline structure (i.e., non calcined sample and samples calcined at lower temperatures in our case) [20,21,71]

It is concluded from Fig. 6e that the nanosheets calcined at 350 ºC boasted the best performance, as they demonstrated the highest capacities across the whole current density range together with the best rate capability. Table S1 in the Electronic Supplementary Material compares the gravimetric capacity values obtained from this sample at several selected current densities with literature data documented for other Co_3O_4 nanomaterials. Concerning the collection of these data, we note that although in a strict sense the concept of capacitance is not applicable to electrodes with a battery-type behavior,[75,76] in many instances capacitance (rather than capacity) values are given for electrodes based on Co_3O_4 materials tested in basic electrolytes, which fall into such a category. However, in these cases capacity values can be readily derived from the reported capacitance data if the potential window is provided, which is most frequently the norm. Overall, it is apparent from Table S1 that the present activated nanosheets exhibited a rather competitive performance, not only in terms of the capacity values themselves but also as regards their retention at high current densities. In particular,

they compared favorably with oxygen vacancy-rich Co_3O_4 nanosheets and reduced mesoporous Co_3O_4 nanowires reported previously, the electrochemical performance of which had been substantially boosted through activation by reduction post-treatment with $NaBH_4$. For example, the capacity of the nanosheets calcined at 350 ºC was 291 mA h g^{-1} at 2 A g^{-1}, compared with values of ~227 and 136 mA h g^{-1} for the oxygen vacancy-rich nanosheets and the reduced mesoporous nanowires, respectively, and their capacity retention was ~92% at 10 A g^{-1} (compared to ~50% for the reduced mesoporous nanowires) and ~88% at 15 A g^{-1} (compared to ~80% for the oxygen vacancy-rich nanosheets).[20,35] These results demonstrate that the direct route proposed here for the preparation of Co_3O_4 nanosheets can afford activated materials with comparable or even better performance than that of similar Co_3O_4 nanomaterials that were activated post-synthesis, which can be beneficial when considering their practical use.

It is reasonable to assume that the different rate capabilities of the investigated materials, as noticed in Fig. 6e, arise from their distinct abilities to allow the conduction of electrons and the (de)intercalation of ions, which are the two basic processes accounting for their charge storage behavior. For example, the highly disordered or even amorphous nature of the non-calcined nanosheets could lead to a poorer rate capability relative to that of their calcined counterparts, as the amorphous structure would be expected to hamper electron conduction in the lattice. To investigate this question, the electrodes were analyzed by the electrochemical impedance spectroscopy (EIS) technique. Fig. 6f shows Nyquist plots derived from the EIS data recorded in the frequency range between 100 kHz and 10 mHz for the different cobalt oxide nanosheet samples, with the inset providing a closer view of the high frequency region of the plots. The latter was characterized by a semicircle profile, the diameter of which [i.e., the

equivalent series resistance (ESR) parameter] provided a measure of the electronic conduction in the materials. As anticipated, the ESR value for the non-calcined nanosheets (7.8 Ω) was larger than those determined for the calcined nanosheets (5.3, 4.5 and 1.8 Ω for the samples calcined at 250, 350 and 450 ºC, respectively), indicative of a relatively impaired electronic conduction in the former material. Having similar numbers of Co(II) sites, the difference in conductivity between the calcined nanosheets can be ascribed to differences in crystallinity due to the calcination process (the higher the calcination temperature, the more structured the samples become and therefore the higher the electrical conductivity). On the other hand, from the lower frequency region of the Nyquist plots we notice that the non-calcined material boasted the most vertical line of all the samples, suggesting a better efficiency towards ion insertion.[37] This result can be understood on the basis of the smaller thickness of the non-calcined nanosheets (~3–5 nm) relative to that of their calcined counterparts (around 10 nm), which implies the former to be more accessible to ion intercalation. Among the activated Co_3O_4 nanosheets, the sample prepared by calcination at 350 ºC exhibited the most vertical line in the higher frequency range, followed by the sample calcined at 450 ºC. Therefore, even though the 350 ºC sample possessed neither the highest electronic conductivity nor the best ion diffusion ability, it probably struck a proper balance between these two key characteristics (it was the second best sample for both), finally resulting in the material with the best overall performance in terms of capacity and rate capability.

2.3.2 Catalytic reduction of nitroarenes

The cobalt oxide nanosheets were also evaluated as catalysts for the reduction of the nitroarenes 4-nitrophenol (4-NP) and 4-nitroaniline (4-NA) to 4-aminophenol (4-AP) and *p*-phenylenediamine (*p*-PDA), respectively, with $NaBH_4$ as the reducing agent, which are reactions of practical relevance in, e.g., the synthesis of certain analgesic

drugs (paracetamol) or dyes.[78,79] Both reactions are thermodynamically feasible but kinetically hindered by substantial activation barriers, thus requiring the use of proper catalysts to make them proceed at significant rates. Although catalysts based on noble metals (Au, Ag, Pt, Pd, etc) have been intensively investigated for this purpose, a recent move towards more abundant and cost-effective alternatives, such as those relying on non-noble metals (e.g., Ni or Cu), has been gaining momentum.[79] In this context, nanostructured Co_3O_4 has been proposed as a suitable non-noble metal-based catalyst for nitroarene reduction, with its activity being mostly attributed to additional Co(II) centers (usually associated to oxygen vacancies in the lattice).[72,80] Having an abundance of the latter, the present nanosheets (both calcined and non-calcined) could be particularly efficient catalysts for such reactions. Their performance was tested by following the evolution of the intensity of optical absorption peaks characteristic of the nitroarenes (see Fig. S9 of the Electronic Supplementary Material).[72,81] Specifically, in the case of 4-NP we monitored the evolution of the peak located at ~400 nm, which is associated to the deprotonated form of this molecule (i.e., the nitrophenoxide anion, generated in the basic medium of $NaBH_4$) and is not present in its reduced counterpart (aminophenoxide anion; Fig. S9a). For 4-NA, we followed its signature peak at ~380 nm, which is absent from *p*-PDA (Fig. S9b). As the intensity of these absorption peaks reflects the concentration of their respective substrate molecules in the reaction medium, it can be used to plot kinetic profiles of the reaction progress.

Representative examples of the kinetic curves recorded for the cobalt oxide nanosheets are given in Fig. 7a (4-NP) and b (4-NA). The profiles were generally seen to decay in an exponential fashion (after an induction period), hence suggesting the reduction reactions to obey a pseudo-first-order kinetic behavior with respect to the substrate concentration.[81] As expected, no reaction was observed to occur in the absence

of the nanosheets, i.e., when the nanosheet dispersion added to the reaction medium was replaced either by pure water or by the supernatant liquid obtained after sedimentation of the dispersed nanosheets through centrifugation, thus confirming their role as the catalytically active component. As shown in Fig. S9, the reaction products (4-AP and *p*-PDA) were detected by UV-vis absorption spectroscopy. Indeed, calibration of their concentration by this technique indicated an aproximatley one-to-one conversion of reagent to the corresponding expected product. To quantify the catalytic activity of the nanosheets, we determined the number of moles of substrate (4-NP or 4-NA) converted per unit time per mole of cobalt present in the nanosheets, the results of which are shown in Fig. 7c. In the calculations, we assumed CoO and Co_3O_4 as the approximate stoichiometric formulas for the non-calcined and calcined samples, respectively. There were not very large differences in activity between the different materials, although the values for the non-calcined nanosheets tended to be somewhat higher than those of their calcined counterparts. This result can be probably ascribed to (1) the smaller thickness of the former, which implies that more surface active sites are potentially available for reaction per unit mass of catalyst, and/or (2) the fact that Co(II) centers, which are assumed to be the catalytically active sites, are relatively more abundant in the non-calcined nanosheets [~100%, almost no Co(III) centers] than in the calcined samples [~55-60% Co(II) and ~40−45% Co(III)]. Nonetheless, concerning the latter possibility we note that the actual catalytic activity of the Co(II) centers in the amorphous lattice of the non-calcined nanosheets could be distinct to that of their counterparts in the (more nanocrystalline) calcined nanosheets, but this point is currently unknown. It could also be argued that the in-situ treatment of the nanosheets with $NaBH_4$ during the catalytic reaction of the nitroarenes could be activating the nanosheets themselves (particularly the calcined ones). However, XPS measurements (data not shown) of nanosheets treated

with $NaBH_4$ showed no significant change in their Co(II)/Co(III) ratios, so we conclude that the materials do not become further activated during the catalytic reaction. The reason for this could be that because the as-prepared nanosheets are already substantially activated, the remaining Co(III) sites could be hard to reduce to Co(II) by a chemical species with a relatively limited reducing ability. At any rate, the nanosheets boasted a competitive performance when compared with previously reported cobalt oxide nanomaterials as well as other materials made up of non-noble metals and/or their oxides, as noticed from catalytic activity data on 4-NP shown in Table S2 of the Electronic Supplementary Material (data on 4-NA with similar catalysts are much less abundant). In most cases, the activity of the nanosheets was significantly higher than that of other nanostructured cobalt oxide catalysts. In particular, it was similar or even higher than that of Co_3O_4 nanoplates of comparable thickness that were activated through a common reduction post-treatment.[72]Also, it is worth noting that the materials could be reused through centrifugation of the suspension and then redispersion of the nanosheets in water. Again, these results bear testament to the efficiency of the present strategy in accessing activated Co_3O_4 without any post-treatment but at the same time exhibiting improved performance towards practical uses. The fact that the non-calcined sample performed better in these experiments than their calcined counterparts (unlike the case of the electrochemical tests) can be ascribed to the relevance of different factors, such as the electrical conductivity or the Co(II) content, that play a role in their behavior towards different uses, While a good electrical conductuvity is key to the nanosheet performance in electrochemical applications, the same is not expected to be the case for the catalytic reactions, where a large number of active Co(II) centers should be the most relevant single factor that determines nanosheet performance. Under such circumstances, the non-calcined nanosheets should possess the better catalytic

activity because they possessed the larger amount of Co(II) sites, as was indeed observed.

2.3.3 Dye adsorption

Finally, owing to their small thickness and hence large surface area, the nanosheets could also act as efficient adsorbents for, e.g., the decontamination of polluted water. To explore such a possibility, we have preliminarily tested the aqueous-phase adsorption of two dyes (methylene blue and methyl orange) onto the cobalt oxide materials. These are charged molecules, which can therefore be favorably adsorbed on the polar surface of the nanosheets through charge-dipole interactions. Fig. 7d shows the corresponding adsorption capacities measured for both the non-calcined and the calcined samples. In most cases, the adsorbed amounts were found to be substantial (~300–900 mg g^{-1}), suggesting that these nanosheets could make good adsorbents for environmental applications. However, as could have probably been expected, the best results were obtained for the non-calcined nanosheets (adsorption capacities around 900 mg g^{-1}), which could be ascribed to their smaller thickness relative to that of their calcined counterparts. Like we noted for the catalysis tests, the nanosheets could be reused, through several centrifugation and redispersion steps in ethanol in order to desorb the dyes. To put these figures into context, they are compared in Table S3 of the Electronic Supplementary Material with adsorption data taken from the literature for a number of metal oxides, including several in nanostructured form, with the same two dyes (we note that data for Co_3O_4 materials could not be found). Overall, the present nanosheets exhibited the best performance from this set of metal oxide materials in terms of the amount of dye that can be taken up, which should warrant more detailed studies in the future to disclose their full potential in this application area.

3. Conclusions

We have demonstrated that activated Co_3O_4 nanosheets having substantial amounts of Co(II) sites can be obtained through a direct synthesis route that circumvents the need of activation (reduction) post-treatments. The strategy based on a general procedure recently developed by Sun *et al.*[41] and relied on an intermediate cobalt oxide material with nanosheet morphology and a highly disordered structure, the calcination of which afforded Co_3O_4 nanosheets boasting Co(II)/Co(III) ratios of ~1.3–1.4, i.e., similar to those achieved for Co_3O_4 nanomaterials activated by reduction post-treatments. These activated nanosheets demonstrated a good potential for use in a number of energy- and environment-related applications. Specifically, they exhibited a competitive performance in their role as an electrode for charge storage in alkaline electrolyte, surpassing many other nanostructured Co_3O_4 materials in terms of both gravimetric capacity and rate capability (including those materials activated post-synthesis). Furthermore, the activated nanosheets were shown to be effective catalysts in the reduction of nitroarenes, with their activity comparing favorably to that of other catalysts based on non-noble metals and/or their oxides, and were also promising adsorbents of dye pollutants from the aqueous phase. For these two latter applications where electrical conductivity is not an issue, the solvothermal nanosheets prepared without any calcination post-treatment, which were thinner and displayed almost exclusively Co(II) sites, offered the best performance. Finally, the present results suggest that the use of these nanosheets in other relevant applications where nanostructured Co_3O_4 is known to have good prospects for development, such as electrocatalysts for the oxygen evolution reaction or electrodes for Li-ion batteries, will be worth exploring in the future.

4. Experimental

4.1. Chemicals and reagents

The following chemicals and reagents were acquired from Sigma-Aldrich and used as received: ethylene glycol, ethanol, hexamethylenetetramine, sodium borohydride, potassium hydroxide, the surfactant Pluronic P123, the dyes methyl orange and methylene blue, the nitroarenes 4-nitrophenol and 4-nitroaniline. Cobalt (II) acetate tetrahydrate was obtained from Alfa Aesar. Ultrapure water (Milli-Q; resistivity: 18.2 MΩ·cm) was used throughout the work.

4.2 Synthesis of activated 2D Co_3O_4 nanosheets

Activated Co_3O_4 nanosheets were prepared by first synthesizing amorphous cobalt oxide nanosheets in the confined 2D space of inverse lamellar micelles of the non-ionic surfactant Pluronic P123 in ethanol/water medium, followed by controlled calcination at a given target temperature.[41] To obtain the amorphous nanosheets, 200 mg of Pluronic P123 were dissolved in 14 mL of a mixed ethanol/water (33/2, v/v) solvent under stirring. Subsequently, 125 mg of cobalt (II) acetate tetrahydrate and 70 mg of hexamethylenetetramine were added to the resulting mixture. After 15 min, a purple-colored solution was obtained, into which 13 mL of ethylene glycol were poured. Under continuous stirring, the purple solution became transparent in about 30 min, following which it was allowed to statically age for 24 h. The aged solution was then transferred to a Teflon-lined autoclave (capacity: 40 mL) and heat-treated at 170 ºC for 2 h. The resulting greenish solid product was thoroughly washed by repeated cycles of centrifugation (2000 *g* for 20 min, J.P. Selecta Meditronic centrifuge in 30 mL tubes) and re-suspension in water and ethanol (3 cycles for each solvent), and finally dried at room temperature under a vacuum. Calcination of this product was accomplished by

heating at different temperatures, namely 250, 350 and 450 ºC, for 2 h under static air conditions (Thermolyne muffle furnace, from Thermo Scientific).

4.3 Characterization techniques

The samples were characterized by UV-vis absorption spectroscopy, field-emission scanning electron microscopy (FE-SEM), scanning transmission electron microscopy (STEM), atomic force microscopy (AFM), X-ray diffraction (XRD), Raman spectroscopy and X-ray photoelectron spectroscopy (XPS). UV-vis absorption spectra were obtained with a double-beam Heλios α spectrophotometer (Thermo Spectronic). FE-SEM and STEM images were recorded on a Quanta FEG 650 apparatus (FEI Company) working at a voltage of 30 kV. Specimens for FE-SEM were directly mounted onto metallic sample holders using double-sided carbon adhesive tape, whereas for STEM the samples were first dispersed in water by bath-sonication for 20 min (J.P. Selecta Ultrasons system, 40 kHz, power ~20 W L^{-1}) and then drop-cast (~10 μL) onto a copper grid (200 square mesh) covered with a thin, continuous carbon film (Electron Microscopy Sciences). AFM imaging was carried out in the tapping mode of operation with a Nanoscope IIIa Multimode microscope (Veeco), using silicon cantilevers with nominal spring constant and resonance frequency of ~40 N m^{-1} and 250-300 kHz, respectively. SiO_2 (300 nm)/Si was employed as a supporting substrate for AFM, onto which an aqueous dispersion of the sample (prepared by bath-sonication) was deposited by drop-casting. XRD patterns were recorded with a D5000 diffractometer (Siemens) at angles (2θ) between 20 and 70º, using Cu K_α radiation (λ = 0.1504 nm) at a step size of 0.02º and time per step of 1 s. Raman spectroscopy was conducted in a LabRam apparatus (Horiba Jobin Yvon) with a laser excitation wavelength of 532 nm. To prevent damage to the samples, a low incident laser power

(0.5 mW) was applied. For XPS, a SPECS apparatus working at a pressure of 10^{-7} Pa and using a non-monochromatic Mg K_α X-ray source (11.81 kV, 100 W) was employed. Specimens for Raman spectroscopy and XPS were prepared in the form of thin films supported onto silver membrane filters (0.2 μm in pore size, 25 mm in diameter, from Sterlitech Corporation), which were prepared by vacuum filtration of the samples dispersed in aqueous medium.

4.4. Applications of the highly activated 2D Co_3O_4 nanosheets

The activated Co_3O_4 nanosheets were tested as electrodes for electrochemical charge storage, as catalysts for the reduction of nitroarenes and as adsorbents for dyes from the aqueous phase.

4.4.1 Electrochemical energy storage

The electrochemical energy storage experiments were carried out in a three-electrode configuration with a Swagelok-type cell, using the Co_3O_4 materials as the working electrode, a commercial activated carbon fiber as the counter electrode, Hg/HgO (1 M NaOH) as the reference electrode and aqueous 6 M KOH as the electrolyte. The working electrode was prepared by drop-casting aqueous dispersions (0.5 mg mL^{-1}) of the activated nanosheets onto circular (~0.8 cm in diameter) graphite foil pieces, which were then allowed to dry under ambient conditions. Typical nanosheet loadings onto the graphite foil support were in the 0.3–0.4 mg cm^{-2} range. The counter electrode was obtained in the form of a paste that incorporated, in addition to the activated carbon fiber, polytetrafluoroethylene as a binder and carbon black as a conductive additive, in a weight ratio of 90:5:5. A circular piece (~1.3 cm in diameter) of nylon membrane filter (0.45 μm of pore size, from Whatman) was used as a separator for the working and counter electrodes. Before the cell was assembled, the working and counter electrodes

as well as the separator were individually soaked in 6 M KOH and vacuum-degassed. Prior to measurements, the assembled cell with the electrolyte was also vacuum-degassed. The measurements were carried out in a VSP potentiostat (Bio-Logic Science Instruments), recording both cyclic voltammograms at different voltage scan rates and galvanostatic charge/discharge curves at different current densities.

4.4.2 Catalytic reduction of nitroarenes

The catalytic activity of the cobalt oxide nanosheets was evaluated in the reduction of two nitroarenes, namely, 4-nitrophenol (4-NP) and 4-nitroaniline (4-NA), in aqueous medium with $NaBH_4$ as the reducing agent. To this end, aqueous solutions (2.105 mL) containing either 4-NP (0.06 mM) or 4-NA (0.06 mM), a certain amount of the nanosheets (typically ~14-24 mg mL^{-1}) and $NaBH_4$ (36 mM) were prepared and immediately transferred to an UV-vis absorption spectrophotometer. Kinetic profiles of the reaction progress were then recorded by monitoring the intensity of an absorption peak characteristic of the substrate molecule (i.e., the peak located at a wavelength of ~400 nm for 4-NP and ~380 nm for 4-NA) over a certain period of time.

4.4.3 Dye adsorption

For the dye adsorption tests, aqueous solutions of the dyes (methylene blue or methyl orange) were mixed with a colloidal suspension of the nanosheets that was obtained by sonicating the as-prepared powder in water, so that the final concentration of the latter in the mixed solution was ~4 mg mL^{-1}. After being gently stirred with a magnetic bar for 24 h, the nanosheets were separated from the solution by centrifugation (20000 *g*, 20 min). This long adsorption time was selected only to ensure the attainment of adsorption equilibrium and allow the determination of maximum adsorbed concentrations, although in actual applications much shorter times would probably suffice (kinetic tests were beyond the scope of this work). Subsequently, the concentration of dye remaining

in the supernatant was determined by UV-vis absorption spectroscopy and compared with that of the starting solution before adsorption, so that the amount of dye taken up by the nanosheets could be finally derived. Dye concentrations were estimated by measuring the intensity of absorption peaks characteristic of the dyes, namely, the peak located at a wavelength of ~660 nm for methylene blue and ~460 nm for methyl orange. To assess the maximum adsorption capacities of the cobalt oxide nanosheets, the starting concentrations of the dyes in the mixed solutions were purposefully chosen to be high, typically between 1 and 4 mg mL^{-1}.

Acknowledgements

Funding by the Spanish Ministerio de Economía y Competitividad (MINECO) and the European Regional Development Fund (ERDF) through project MAT2015-69844-R is gratefully acknowledged. We are also grateful to Plan de Ciencia, Tecnología e Innovación 2013-2017 del Principado de Asturias and the ERDF for partial funding through project GRUPIN14-056. J.M.M. and S.G-D. are grateful to the Spanish Ministerio de Educación, Cultura y Deporte (MECD) and MINECO, respectively, for their pre-doctoral contracts (FPU14/00792 and BES/2016 077830, respectively).

Electronic Supplementary Material: Supplementary material on the mechanism of formation of the cobalt oxides, digital photograph of pure cobalt hydroxide, additional XPS characterization of the materials, standard powder diffraction pattern of crystalline Co_3O_4, BET surface and total pore volume of the materials as calculated form N_2 adsorption isotherms acquired at -196 °C, on electrochemical charge storage experiments for the non-calcined nanosheets and the nanosheets calcined at 250 and 450 ºC, as well as the UV-vis absorption spectra of the reactants and the products of the

catalytic reduction of nitroarenes assayed in this work, and data from the literature on the performance of similar materials in the different applications assayed in this work to put our results into context is available.

References

[1] Ferrari, A. C.; Bonaccorso, F.; Fal'ko, V.; Novoselov, K. S.; Roche, S.; Boggild, P.; Borini, S.; Koppens, F. H. L.; Palermo, V.; Pugno, N. et al. Science and technology roadmap for graphene, related two-dimensional crystals, and hybrid systems. *Nanoscale* **2015**, *7*, 4598-4810.

[2] Ng, V.M.H.; Huang, H.; Zhou, K.; Lee, P. S.; Que, W.; Xu, J.Z.; Kong, L.B. Recent progress in layered transition metal carbides and/or nitrides (Mxenes) and their composites: synthesis and applications. *J. Mater. Chem. A* **2017**, *5*, 3039-3068.

[3] Zhang, K.; Feng, Y.; Wang, F.; Yang, Z.; Wang, J. Two dimensional hexagonal boron nitride (2D-hBN): synthesis, properties and applications. *J. Mater. Chem. C* **2017**, *5*, 11992-12022.

[4] Samadi, M.; Sarikhani, N.; Zirak, M.; Zhang, H.; Zhang, H.-L.; Moshfegh, A. Z. Group 6 transition metal dichalcogenide nanomaterials: synthesis, applications and future perspectives. *Nanoscale Horiz.* **2018**, *3*, 90-204.

[5] Zhang, S.; Guo, S.; Chen, Z.; Wang, Y.; Gao, H.; Gómez-Herrero, J.; Ares, P.; Zamora, F.; Zhu, Z.; Zeng, H. Recent progress in 2D group-VA semiconductors: from theory to experiment. *Chem. Soc. Rev.* **2018**, *47*, 982-1021.

[6] Tan, C.; Zhang, H. Wet-chemical synthesis and applications of non-layer structured two-dimensional nanomaterials. *Nat. Commun.* **2015**, *6*, 7873.

[7] Wang, F.; Wang, Z.; Shifa, T. A.; Wen, Y.; Wang, F.; Zhan, X.; Wang, Q.; Xu, K.; Huang, Y.; Yin, L. et al. Two-dimensional non-layered materials: synthesis, properties and applications. *Adv. Funct. Mater.* **2017**, *27*, 1603254.

[8] Dou, Y.; Zhang, L.; Xu, X.; Sun, Z.; Liao, T.; Dou, S. X. Atomically thin non-layered nanomaterials for energy storage and conversion. *Chem. Soc. Rev.* **2017**, *46*, 7338-7373.

[9] Yang, W.; Zhang, X.; Xie, Y. Advances and challenges in chemistry of two-dimensional nanosheets. *Nano Today* **2016**, *11*, 793-816.

[10] Tan, H. T.; Sun, W.; Wang, L.; Yan, Q. 2D transition metal oxides/hydroxides for energy-storage applications. *ChemNanoMat* **2015**, *2*, 562-577.

[11] Chen, P.-Y.; Liu, M.; Valentin, T. M.; Wang, Z.; Steinberg, R. S.; Sodhi, J.; Wong, I. Y.; Hurt, R. H. Hierarchical metal oxide topographies replicated from highly textured graphene oxide by intercalation templating. *ACS Nano* **2016**, *10*, 10869-10879.

[12] Kong, X.; Liu, Q.; Zhang, C.; Peng, Z.; Chen, Q. Elemental two-dimensional nanosheets beyond graphene. *Chem. Soc. Rev.* **2017**, *46*, 2127-2157.

[13] Liu, M.; Chen, P.-Y.; Hurt, R. H. Graphene inks as versatile templates for printing tiled metal oxide crystalline films. *Adv. Mater.* **2018**, *30*, 1705080.

[14] Sun, Y.; Gao, S.; Lei, F.; Liu, J.; Liang, L.; Xie, Y. Atomically-thin non-layered cobalt oxide porous sheets for highly efficient oxygen-evolving electrocatalysts. *Chem. Sci.* **2014**, *5*, 3976-3982.

[15] Du, S.; Ren, Z.; Qu, Y.; Wu, J.; Xi, W.; Zhu, J.; Fu, H. Co_3O_4 Nanosheets as a high-performance catalyst for oxygen evolution proceeding via a double two-electron process. *Chem. Commun*. **2016**, *52*, 6705-6708.

[16] Cai, Z.; Bi, Y.; Hu, E.; Liu, W.; Dwarica, N.; Tian, Y.; Li, X.; Kuang, Y.; Li, Y.; Yang, X.-Q et al. Single-crystalline ultrathin Co_3O_4 nanosheets with massive vacancy defects for enhanced electrocatalysis. *Adv. Energy Mater.* **2018**, *8*, 1701694.

[17] Yuan, C.; Yang, L.; Hou, L.; Shen, L.; Zhang, X.; Lou, X. W. Growth of ultrathin mesoporous Co_3O_4 nanosheet arrays on Ni foam for high-performance electrochemical capacitors. *Energy Environ. Sci.* **2012**, *5*, 7883-7887.

[18] Feng, C.; Zhang, J.; He, Y.; Zhong, C.; Hu, W.; Liu, L.; Deng, Y. Sub-3 nm Co_3O_4 nanofilms with enhanced supercapacitor properties. *ACS Nano* **2015**, *9*, 1730-1739.

[19] Fan, H.; Quan, L.; Yuan, M.; Zhu, S.; Wang, K.; Zhong, Y.; Chang, L.; Shao, H.; Wang, J.; Zhang, J. et al. Thin Co_3O_4 nanosheet array on 3D porous graphene/nickel foam as a binder-free electrode for high-performance supercapacitors. *Electrochim. Acta* **2016**, *188*, 222-229.

[20] Xiang, K.; Xu, Z.; Qu, T.; Tian, Z.; Zhang, Y.; Wang, Y.; Xie, M.; Guo, X.; Ding, W.; Guo, X. Two dimensional oxygen-vacancy-rich Co_3O_4 nanosheets with excellent supercapacitor performances. *Chem. Commun.* **2017**, *53*, 12410-12413.

[21] Xiao, Z.; Fan, L.; Xu, B.; Zhang, S.; Kang, W.; Kang, Z.; Lin, H.; Liu, X.; Zhang, S.; Sun, D. Metal–organic framework-derived metal oxide embedded in nitrogen-doped graphene network for high-performance lithium-ion batteries. *ACS Appl. Mater. Interfaces* **2017**, *9*, 41827-41836.

[22] Son, M. Y.; Kim, J. H.; Kang, Y. C. Study of Co_3O_4 mesoporous nanosheets prepared by a simple spray-drying process and their electrochemical properties as anode material for lithium secondary batteries. *Electrochim. Acta* **2014**, *116*, 44-50.

[23] Wang, B.; Lu, X.-Y.; Tang, Y.; Ben, W. General polyethyleneimine-mediated synthesis of ultrathin hexagonal Co_3O_4 nanosheets with reactive facets for lithium-ion batteries. *ChemElectroChem* **2016**, *3*, 55-65.

[24] AbdelHamid, A. A.; Yu, Y.; Yang, J.; Ying, J. Y. Generalized synthesis of metal oxide nanosheets and their application as Li-ion battery anodes. *Adv. Mater.* **2017**, *29*, 1701427.

[25] Yao, Y.; Zhu, Y.; Zhao, S.; Shen, J.; Yang, X.; Li, C. Magnetic electrodeposition of hierarchical cobalt oxide nanostructure from spent lithium-ion batteries: its application as supercapacitor electrode. *ACS Appl. Energy Mater.* **2018**, *1*, 1239-1251.

[26] Wang, G.; Yang, Y.; Han, D.; Li, Y. Oxygen defective metal oxides for energy conversion and storage. *Nano Today* **2017**, *13*, 23-39.

[27] Kou, T.; Yao, B.; Liu, T.; Li, Y. Recent advances in chemical methods for activating carbon and metal oxide based electrodes for supercapacitors. *J. Mater. Chem. A* **2017**, *5*, 17151-17173.

[28] Kalantar-zadeh, K.; Ou, J. Z.; Daeneke, T.; Mitchell, A.; Sasaki, T.; Fuhrer, M. S. Two dimensional and layered transition metal oxides. *Appl. Mater. Today* **2016**, *5*, 73-89.

[29] Zhang, G.; Xiao, X.; Li, B.; Gu, P.; Xue, H.; Pang, H. transition metal oxides with one-dimensional/one-dimensional-analogue nanostructures for advanced supercapacitors. *J. Mater. Chem. A* **2017**, *5*, 8155-8186.

[30] Kong, D.; Ren, W.; Cheng, C.; Wang, Y.; Huang, Z.; Yang, H. Y. Three–dimensional $NiCo_2O_4$@polypyrrole coaxial nanowire arrays on carbon textiles for high-performance flexible asymmetric solid–state supercapacitor. *ACS Appl. Mater. Interfaces* **2015**, *7*, 21334−21346.

[31] Sahoo, S.; Shim, J.-J. Facile synthesis of three-dimensional ternary $ZnCo_2O_4$/reduced graphene oxide/NiO composite film on nickel foam for next generation supercapacitor electrodes. *ACS Sustainable Chem. Eng.* **2017**, *5*, 241−251.

[32] Young, C.; Salunkhe, R. R.; Alshehri, S. M.; Ahamad, T.; Huang, Z.; Henzie, J.; Yamauchi, Y. High energy density supercapacitors composed of nickel cobalt oxide nanosheets on nanoporous carbon nanoarchitectures. *J. Mater. Chem. A* **2017**, *5*, 11834-11839.

[33] Kaneti, Y. V.; Salunkhe, R. R.; Septiani, N.L.W.; Young, C.; Jiang, X. C.; He, Y. B.; Kang, Y. M.; Sugahara, Y.; Yamauchi, Y. General template-free strategy for fabricating mesoporous two-dimensional mixed oxide nanosheets via self-deconstruction/reconstruction of monodispersed metal glycerate nanospheres. *J. Mater. Chem. A* **2018**, *6*, 5971-5983.

[34] Li, X.; Wang, L.; Shi, J.; Du, N.; He, G. Multishelled nickel−cobalt oxide hollow microspheres with optimized compositions and shell porosity for high-performance pseudocapacitors. *ACS Appl. Mater. Interfaces* **2016**, *8*, 17276−17283.

[35] Wang, Y.; Zhou, T.; Jiang, K.; Da, P.; Peng, Z.; Tang, J.; Kong, B.; Cai, W.-B.; Yang, Z.; Zheng, G. Reduced mesoporous Co_3O_4 nanowires as efficient water oxidation electrocatalysts and supercapacitor electrodes. *Adv. Energy Mater.* **2014**, *4*, 1400696.

[36] Chen, H.; Yang, M.; Tao, S.; Chen, G. Oxygen vacancy enhanced catalytic activity of reduced Co_3O_4 towards p-nitrophenol reduction. *Appl. Catal. B: Environ.* **2017**, *209*, 648-656.

[37] Yang, S.; Liu, Y.; Hao, Y.; Yang, X.; Goddard, W. A.; Zhang, X. L.; Cao, B. Oxygen-vacancy abundant ultrafine Co_3O_4/graphene composites for high-rate supercapacitor electrodes. *Adv. Sci.* **2018**, *5*, 1700659.

[38] Yang, M.-Q.; Wang, J.; Wu, H.; Ho, G. W. Noble metal-free nanocatalysts with vacancies for electrochemical water splitting. *Small* **2018**, *14*, 1703323.

[39] Wei, R.; Fang, M.; Dong, G.; Lan, C.; Shu, L.; Zhang, H.; Bu, X.; Ho, J. C. High-index faceted porous Co_3O_4 nanosheets with oxygen vacancies for highly efficient water oxidation. *ACS Appl. Mater. Interfaces* **2018**, *10*, 7079-7086.

[40] Qiao, L.; Swihart, M. T. Solution-phase synthesis of transition metal oxide nanocrystals: morphologies, formulae, and mechanisms. *Adv. Colloid Interface Sci.* **2017**, *244*, 199-266.

[41] Sun, Z.; Liao, T.; Dou, Y.; Hwang, S. M.; Park, M.-S.; Jiang, L.; Kim, J. H.; Dou, S. X. Generalized self-assembly of scalable two-dimensional transition metal oxide nanosheets. *Nat. Commun.* **2014**, *5*, 3813.

[42] Xu, L.; Jiang, Q.; Xiao, Z.; Li, X.; Huo, J.; Wang, S.; Dai, L. Plasma-engraved Co_3O_4 nanosheets with oxygen vacancies and high surface area for the oxygen evolution reaction. *Angew. Chem. Int. Ed.* **2016**, *55*, 5277-5281.

[43] Zhou, Y.; C.-K. Dong, C.-K.; L.-L. Han, L.-L.; J. Yang, J.; X.-W. Du, X.-D. Top-down preparation of active cobalt oxide catalyst. *ACS Catal.* **2016**, *6*, 6699-6703.

[44] Shim, H.-S.; Shinde, V. R.; Kim, H. J.; Sung, Y.-E.; Kim, W. B. Porous cobalt oxide thin films from low temperature solution phase synthesis for electrochromic electrode. *Thin Solid Films* **2008**, *516*, 8573-8578.

[45] Farhadi, S.; Safabakhsh, J.; Zaringhadam, P. Synthesis, Characterization, and investigation of optical and magnetic properties of cobalt oxide (Co_3O_4) nanoparticles. *J. Nanostruct. Chem.* **2013**, *3*, 69.

[46] Kang, M.; Zhou, H. Facile synthesis and structural characterization of Co_3O_4 nanocubes. *AIMS Mater. Sci.* **2015**, *2*, 16-27.

[47] Samal, R.; Dash, B.; Sarangi, C. K.; Sanjay, K.; Subbaiah, T.; Senanayake, G.; Minakshi, M. Influence of synthesis temperature on the growth and surface morphology of Co_3O_4 nanocubes for supercapacitor applications. *Nanomaterials* **2017**, *7*, 356.

[48] Ma, K.; Liu, F.; Yuan, Y. F.; Liu, X. Q.; Wang, J.; Xie, J.; Cheng, J. P. CoO microspheres and metallic Co evolved from Hexagonal α-$Co(OH)_2$ plates in a hydrothermal process for lithium storage and magnetic applications. *Phys. Chem. Chem. Phys.* **2018**, *20*, 595-604.

[49] Nethravathi, C.; Sen, S.; Ravishankar, N.; Rajamathi, M.; Pietzonka, C.; Harbrecht, B. Ferrimagnetic nanogranular Co_3O_4 through solvothermal decomposition of colloidally dispersed monolayers of α-cobalt hydroxide. *J. Phys. Chem. B* **2005**, *109*, 11468-11472.

[50] Dou, Y.; Zhang, L.; Xu, J.; He, C.-T.; Xu, X.; Sun, Z.; Liao, T.; Nagy, B.; Liu, P.; Dou, S. X. Manipulating the architecture of atomically thin transition metal (hydr)oxides for enhanced oxygen evolution catalysis. *ACS Nano* **2018**, *12*, 1878−1886.

[51] N. N. Greenwood, A. Earnshaw. Chemistry of the elements. Ch. 26: Cobalt, rhodium and iridium., p. 1296. Pergamon Press. Oxford, 1984.

[52] Ma, R.; Liu, Z.; Takada, K.; Fukuda, K.; Ebina, Y.; Bando, Y.; Sasaki, T. Tetrahedral Co(II) coordination in α-type cobalt hydroxide: Rietveld refinement and X-ray absorption spectroscopy. *Inorg. Chem.* **2006**, *45*, 3964-3969.

[53] Al-Ghoul, M.; El-Rassy, H.; Coradin, T.; Mokalled, T. Reaction–diffusion based co-synthesis of stable α- and β-cobalt hydroxide in bio-organic gels. *J. Cryst. Growth* **2010**, *312*, 856-862.

[54] Schneiderová, B.; Demel, J.; Pleštil, J.; Tarábková, H.; Bohuslav, J.; Lang, K. Electrochemical performance of cobalt hydroxide nanosheets formed by the

delamination of layered cobalt hydroxide in water. *Dalton Trans.* **2014**, *43*, 10484-10491.

[55] Lyu, F.; Bai, Y.; Wang, Q.; Wang, L.; Zhang, X.; Yin, Y. Phase-controllable synthesis of cobalt hydroxide for electrocatalytic oxygen evolution. *Dalton Trans.* **2017**, *46*, 10545-10548.

[56] Kim, T. W.; Oh, E.-J.; Jee, A.-Y.; Lim, S. T.; Park, D. H.; Lee, M.; Hyun, S.-H.; Choy, J.-H.; Hwang, S.-J. Soft-Chemical exfoliation route to layered cobalt oxide monolayers and its application for film deposition and nanoparticle synthesis. *Chem. Eur. J.* **2009**, *15*, 10752-10761.

[57] Kundu, S.; Jayachandran, M. Shape-selective synthesis of non-micellar cobalt oxide (CoO) nanomaterials by microwave irradiations. *J. Nanopart. Res.* **2013**, *15*, 1543.

[58] Ma, R.; Liu, Z.; Takada, K.; Fukuda, K.; Ebina, Y.; Bando, Y.; Sasaki, T. Tetrahedral Co(II) Coordination in α-type Cobalt Hydroxide: Rietveld Refinement and X-Ray Absorption Spectroscopy. *Inorg. Chem.* **2006**, *45*, 3964-3969.

[59] Gallant, D.; Pézolet, M.; Simard, S. Optical and physical properties of cobalt oxide films electrogenerated in bicarbonate aqueous media. *J. Phys. Chem. B* **2006**, *110*, 6871-6880.

[60] Alrehaily, L. M.; Joseph, J. M.; Wren, J. C. Radiation-induced formation of Co_3O_4 nanoparticles from Co^{2+}(aq): Probing the Kinetics Using Radical Scavengers. *Phys. Chem. Chem. Phys.* **2015**, *17*, 24138-24150.

[61] Li, Y.; Qiu, W.; Qin, F.; Fang, H.; Hadjiev, V. G.; Litvinov, D.; Bao, J. Identification of cobalt oxides with Raman scattering and Fourier transform infrared spectroscopy. *J. Phys. Chem. C* **2016**, *120*, 4511-4516.

[62] Rivas-Murias, B.; Salgueiriño, V. Thermodynamic CoO– Co_3O_4 crossover using Raman spectroscopy in magnetic octahedron-shaped nanocrystals. *J. Raman Spectrosc.* **2017**, *48*, 837-841.

[63] Li, H. B.; Yu, M. H.; Lu, X. H.; Liu, P.; Liang, Y.; Xiao, J.; Tong, Y. X.; Yang, G. W. Amorphous cobalt hydroxide with superior pseudocapacitive performance. *ACS Appl. Mater. Interfaces* **2014**, *6*, 745-749.

[64] Choi, H. C.; Jung, Y. M.; Noda, I.; Kim, S. B. A Study of the mechanism of the electrochemical reaction of lithium with CoO by two-dimensional soft X-ray absorption spectroscopy (2D XAS), 2D Raman, and 2D heterospectral XAS−Raman correlation analysis. *J. Phys. Chem. B* **2003**, *107*, 5806-5811.

[65] Ravindra, A. V.; Behera, B. C.; Padhan, P. Laser induced structural phase transformation of cobalt oxides nanostructures. *J. Nanosci. Nanotechnol.* **2014**, *14*, 5591-5595.

[66] Johansson, G.; Hedman, J.; Berndtsson, A.; Klasson, M.; Nilsson, R. Calibration of electron spectra. *J. Electron Spectrosc.* **1973**, *2*, 295.

[67] Cochran, S. J.; Larkins, F. P. Surface reduction of some transition-metal oxides. an X-Ray photoelectron spectroscopic study of iron, cobalt, nickel and zinc oxides. *J. Chem. Soc., Faraday Trans. 1*, **1985**, *81*, 2179-2190

[68] Chuang, T. J.; Bridle, C. R.; Rice, D. W. Interpretation of the X-Ray photoemission spectra of cobalt oxides and cobalt oxide surfaces. *Surface Science* **1976**, *59*, 413-429.

[69] Wang, G.; Shen, X.; Horvat, J.; Wang, B.; Liu, H.; Wexler, D.; Yao, J. Hydrothermal synthesis and optical, magnetic, and supercapacitance properties of nanoporous cobalt oxide nanorods. *J. Phys. Chem. C* **2009**, *113*, 4357-4361.

[70] Gao, S.; Sun, Z.; Liu, W.; Jiao, X.; Zu, X.; Hu, Q.; Sun, Y.; Yao, T.; Zhang, W.; Wei, S. et al. atomic layer confined vacancies for atomic-level insights into carbon dioxide electroreduction. *Nat. Commun*. **2017**, *8*, 14503.

[71] Cheng, G.; Kou, T.; Zhang, J.; Si, C.; Gao, H.; Zhang, Z. O_2^{2-}/O^- functionalized oxygen-deficient Co_3O_4 Nanorods as high performance supercapacitor electrodes and electrocatalysts towards water splitting. *Nano Energy* **2017**, *38*, 155-166.

[72] Tian, X.; Sun, X.; Jiang, Z.; Jiang, Z.-J.; Hao, X.; Shao, D.; Maiyalagan, T. Exploration of the active center structure of nitrogen-doped graphene for control over the growth of Co_3O_4 for a high-performance supercapacitor. *ACS Appl. Energy Mater.* **2018**, *1*, 143-153.

[73] Yan, K.-L.; Qin, J.-F.; Lin, J.-H.; Dong, B.; Chi, J.-Q.; Liu, Z.-Z.; Dai, F.-N.; Chai, Y.-M.; Liu, C.-G. Probing the active sites of Co_3O_4 for the acidic oxygen evolution reaction by modulating the Co^{2+} /Co^{3+} ratio. *J. Mater. Chem. A* **2018**, *6*, 5678-5686.

[74] Wang, H.-Y.; Hung, S.-F.; Chen, H.-Y.; Chan, T.-S.; Chen, H. M.; Liu, B. In operando identification of geometrical-site-dependent water oxidation activity of spinel Co_3O_4. *J. Am. Chem. Soc.* **2016**, *138*, 36-39.

[75] Brousse, T.; Bélanger, D.; Long, J. W. To be or not to be pseudocapacitive? *J. Electrochem. Soc.* **2015**, *162*, A5185-A5189.

[76] Gogotsi, Y.; Penner, R. M. Energy storage in nanomaterials – capacitive, pseudocapacitive, or battery-like? *ACS Nano* **2018**, *12*, 2081-2983.

[77] Tan, H.; Liu, Z.; Chao, D.; Hao, P.; Jia, D.; Sang, Y.; Liu, H.; Fan, H. J. Partial nitridation-induced electrochemistry enhancement of ternary oxide nanosheets for fiber energy storage device. *Adv. Energy Mater.* **2018**, *8*, 1800685.

[78] Aditya, T.; Pal, A.; Pal, T. Nitroarene reduction: a trusted model reaction to test nanoparticle catalysts. *Chem. Commun.* **2015**, *51*, 9410-9431.

[79] Hu, H.; Xin, J. H.; Hu, H.; Wang, X.; Miao, D.; Liu, Y. Synthesis and stabilization of metal nanocatalysts for reduction reactions – a review. *J. Mater. Chem. A* **2015**, *3*, 11157-11182.

[80] Mandlimath, T. R.; Gopal, B. Catalytic activity of first row transition metal oxides in the conversion of p-nitrophenol to p-aminophenol. *J. Mol. Catal. A: Chem.* **2011**, *350*, 9-15.

[81] Ayán-Varela, M.; Paredes, J. I.; Guardia, L.; Villar-Rodil, S.; Munuera, J. M.; Díaz- González, M.; Fernández-Sánchez, C.; Martínez-Alonso, A.; Tascón, J. M. D. Achieving Extremely Concentrated Aqueous Dispersions of Graphene Flakes and Catalytically Efficient Graphene-Metal Nanoparticle Hybrids with Flavin Mononucleotide as a High Performance Stabilizer. *ACS Appl. Mater. Interfaces* **2015**, *7*, 10293-10307.

Figure Captions

Figure 1. Schematic chart depicting two different strategies to access activated Co_3O_4 nanosheets, namely, through a post-synthesis reduction treatment (path A) or via a direct route that avoids reduction post-treatments (path B).

Figure 2. (a) Digital photograph of the as-prepared solvothermal product (left) and the same product after being dispersed in water by mild sonication (right). (b,c) FE-SEM images of the as-prepared solvothermal solid highlighting its stratified nature. (d,e) STEM (d) and AFM (e) images of individual nanosheets detached from the solvothermal solid. In (e), a line profile taken along the marked white line is shown in black color superimposed on the AFM image.

Figure 3. Spectroscopic characterization of the as-prepared solvothermal nanosheets: (a) UV-vis absorption spectrum of the nanosheets dispersed in water, (b) Raman spectrum, and (c,d) high resolution XPS Co $2p_{3/2}$ (c) and O 1s (d) core-level spectra.

Figure 4. FE-SEM (a-c) and STEM (d-i) images of the solvothermal nanosheets after calcination at 250 (a,d,g) 350 (b,e,h) and 450 ºC (c,f,i).

Figure 5. Structural and spectroscopic characterization of the calcined nanosheets: (a) X-ray diffractograms, (b) Raman spectra, (c) UV-vis absorption spectra, and (d,e) high resolution XPS Co $2p_{3/2}$ (d) and O 1s (e) core-level spectra.

Figure 6. Electrochemical testing of the nanosheets in 6 M KOH electrolyte: (a) cyclic voltammograms recorded at a potential scan rate of 10 mV s^{-1} for the non-calcined and calcined nanosheets, (b) cyclic voltammograms recorded at different scan rates between 3 and 500 mV s^{-1} for the nanosheets calcined at 350 ºC (inset: magnitude of the oxidation peak current vs square root of the potential scan rate), (c) galvanostatic charge-discharge curves recorded at a current density of 10 A g^{-1} for the non-calcined and calcined nanosheets, (d) galvanostatic charge-discharge curves recorded at different current densities between 1 and 60 A g^{-1} for the nanosheets calcined at 350 ºC, (e) gravimetric capacity of the non-calcined and calcined nanosheets measured as a function of current density, and (f) electrochemical impedance spectra of the non-calcined and calcined nanosheets (inset: detailed view of the high frequency region of the spectra).

Figure 7. (a,b) Kinetic profiles recorded for the reduction of 4-NP (a) and 4-NA (b) with $NaBH_4$ using the non-calcined and calcined nanosheets catalysts. (c) Catalytic activities of the non-calcined and calcined nanosheets towards 4-NP (black columns) and 4-NA reduction with $NaBH_4$ (green columns), determined as the number of moles of substrate (4-NP or 4-NA) converted per unit time per mole of cobalt present in the nanosheets. (d) Measured adsorption capacities of the non-calcined and calcined nanosheets towards methylene blue (blue columns) and methyl orange (orange columns) from the aqueous phase.

Figure 1.

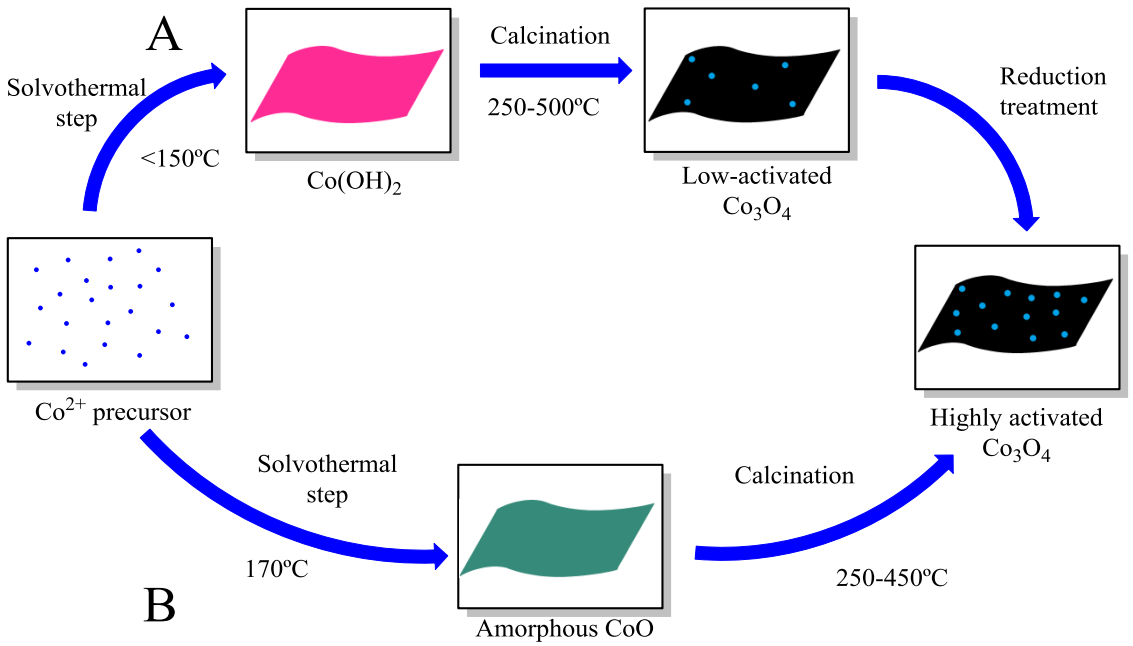

Figure 2.

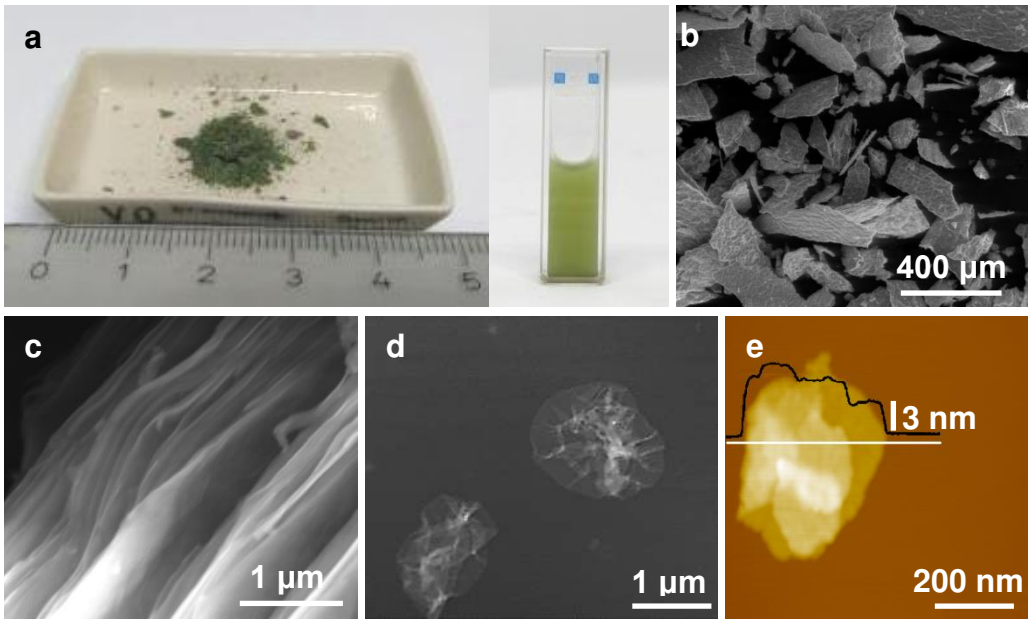

Figure 3.

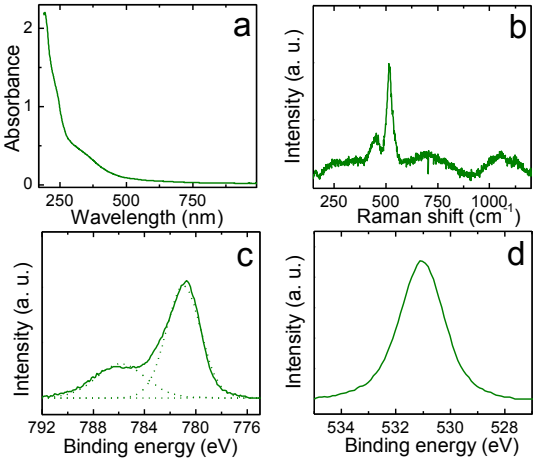

Figure 4.

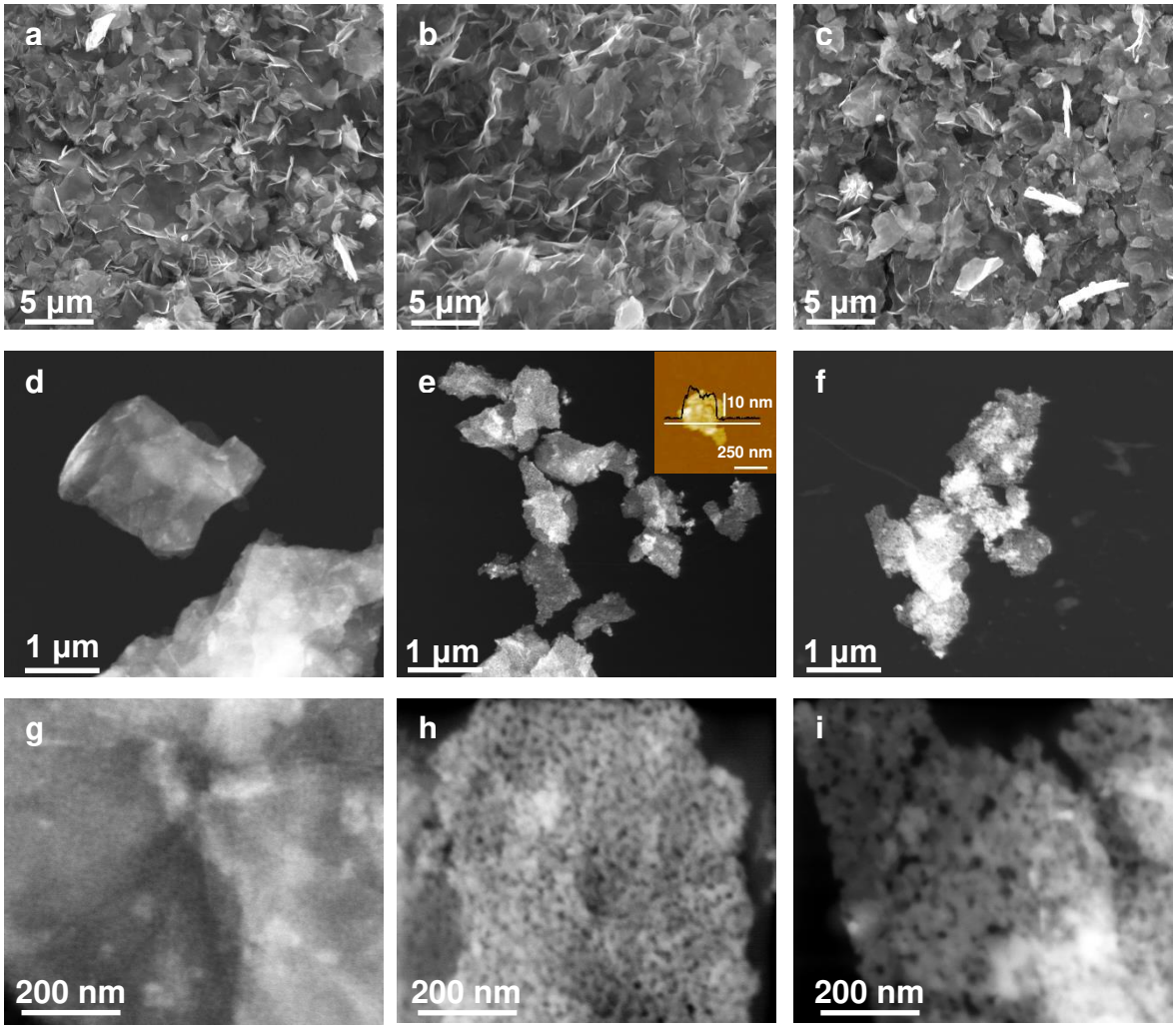

Figure 5.

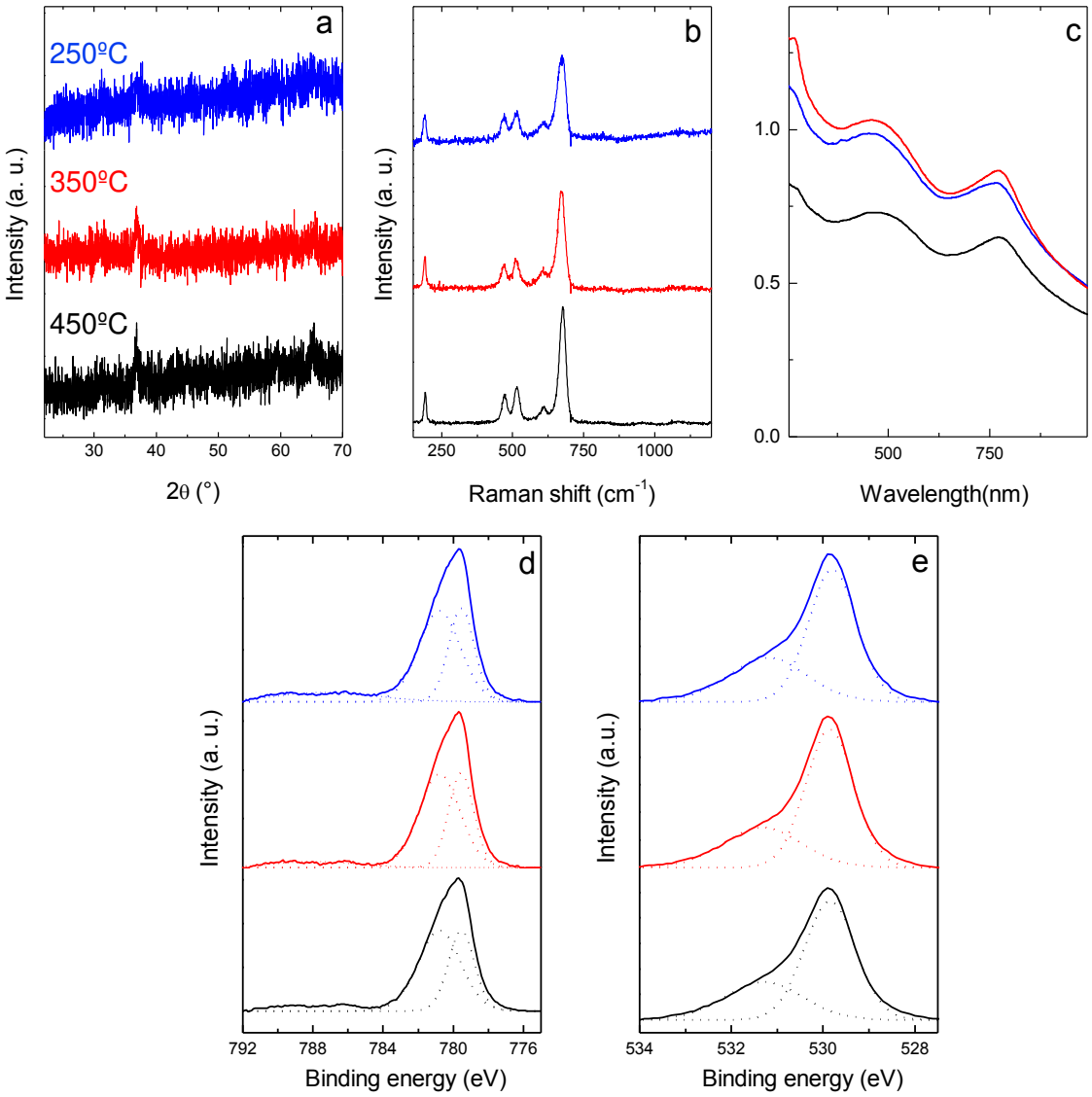
a
250ºC
350ºC
450ºC
Intensity (a. u.)
30
40
50
60
70
2θ (°)
b
Intensity (a. u.)
250
500
750
1000
Raman shift (cm-1)
c
1.0
0.5
0.0
500
750
Wavelength(nm)
d
Intensity (a. u.)
792
788
784
780
776
Binding energy (eV)
e
Intensity (a.u.)
534
532
530
528
Binding energy (eV)

Figure 6.

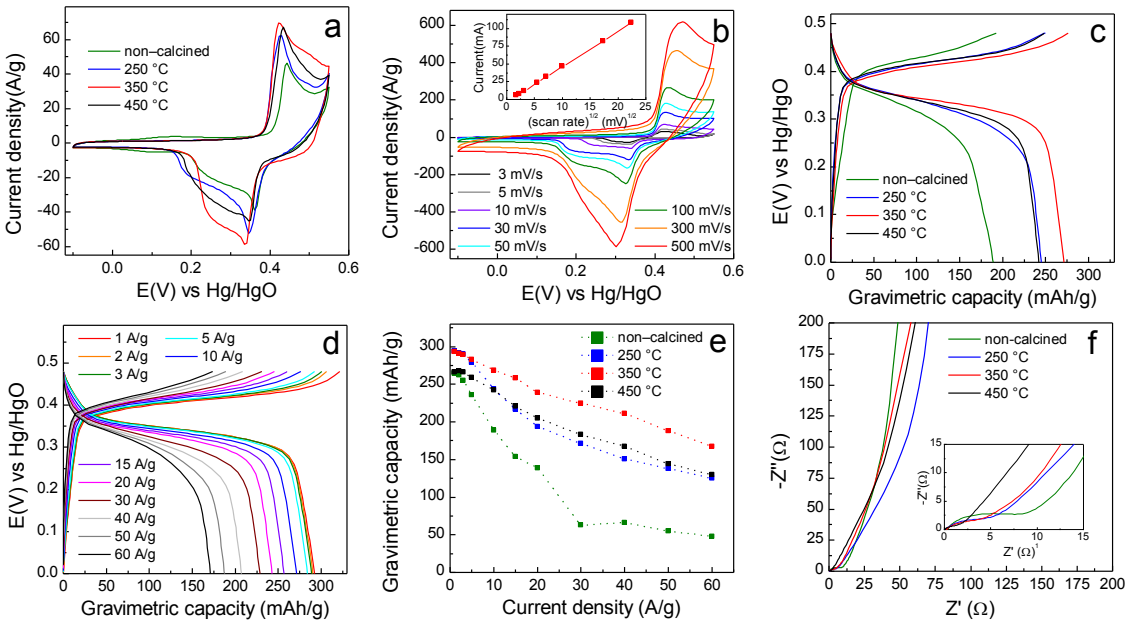

Figure 7.